Multi-Scale Simulation of a Novel Integrated Reactor for Hydrogen Production by Ammonia Decomposition

Sebastian Blauth, Julie Damay, Sebastian Osterroth, Christian Leithäuser, Christian Hofmann, Gunther Kolb, Martin Wichert, Konrad Steiner, Michael Bortz

Multi-Scale Simulation of a Novel Integrated Reactor for Hydrogen Production by Ammonia Decomposition

Dr. Sebastian Blauth[1], Dr.-Ing. Julie Damay[1,*], Dr. Sebastian Osterroth[1], Dr. Christian Leithäuser[1], Christian Hofmann[2], Dr.-Ing. Gunther Kolb[2], Martin Wichert[2], Dr. Konrad Steiner[1], and Prof. Dr. Michael Bortz[1]

A novel reactor concept for ammonia decomposition utilizing tail gas from a purification unit as heat supply is presented. The designed micro-structured reactor integrates both endothermic ammonia decomposition and exothermic tail gas combustion. The reactor and corresponding process are simulated using a mathematical multi-scale model, which combines the results of multiple detailed computational fluid dynamics simulations into a fast surrogate model. The latter is coupled with a process simulation software via a so-called container to simulate the entire process. The efficiency of the presented reactor concept is determined and benefits over alternative approaches are highlighted.

Keywords: Ammonia decomposition; CFD simulation; Hydrogen production; Multi-scale simulation; Process simulation

Author affiliations

[1] Fraunhofer Institute for Industrial Mathematics ITWM, Fraunhofer-Platz 1, 67663 Kaiserslautern, Germany

[2]Fraunhofer Institute for Microengineering and Microsystems IMM, Carl-Zeiss-Str. 18-20, 55129 Mainz, Germany

Email corresponding author: julie.damay@itwm.fraunhofer.de

ORCID iDs of the authors:

0000-0001-9173-0866 (Sebastian Blauth)

0000-0001-8169-2907 (Michael Bortz)

0000-0002-6031-9457 (Julie Damay)

0000-0003-2392-1278 (Gunther Kolb)

0000-0002-4542-1525 (Christian Hofmann)

0000-0001-8936-9805 (Christian Leithäuser)

0000-0001-9702-521X (Sebastian Osterroth)

0000-0002-8277-3319 (Martin Wichert)

1 Introduction

Nowadays, it is widely accepted that extreme meteorological conditions are caused or at least significantly enhanced by human-induced climate change due to greenhouse gas emissions [1]. The continuous increase of the greenhouse gas carbon dioxide in the atmosphere is mainly caused by combustion of fossil fuels [2]. Therefore, there is growing interest in alternatives to fossil fuels. Hydrogen is a promising alternative due to its high energy density, the absence of COx species when combusted, and its good long-term storage stability. However, the fluctuating nature of renewable energy sources makes on-demand hydrogen production challenging [3], leading to the need to import hydrogen from countries with abundant solar and wind resources. To overcome the challenges of hydrogen transportation, ammonia is favored as a hydrogen carrier due to its higher volumetric energy density and established infrastructure [4].

Energy generation from ammonia is possible either by direct conversion [5] or through hydrogen extraction with the help of cracking technologies [6–9]. In this paper, we focus on the latter. A high purity of the recovered hydrogen is important for many applications. For example, for low-temperature proton-exchange membrane (PEM) fuel cells, an ammonia concentration of less than 0.1 ppm is required to ensure high efficiency of the cells and prevent irreversible damage to their catalyst and membranes [10]. Therefore, hydrogen purification technologies such as pressure swing adsorption (PSA) [11] or metal membrane technology (MMT) [12] need to be applied.

Ammonia decomposition plants can be divided into different categories depending on their thermal power supply for the endothermic cracking reaction. Electrically heated reactors, which are available as laboratory equipment [13] as well as large-scale chemical plants [14], have been developed. Another way of providing thermal power for the endothermic cracking reaction is to use off-gases from the purification process to achieve high efficiency. These approaches are used, e.g., in [15–18], where fuel cell anode off-gas and retentate from a membrane separation unit are used to power the ammonia cracker.

In this paper, we present a novel ammonia cracking reactor utilizing tail gas from a PSA unit as heat supply. The reactor integrates both endothermic ammonia decomposition and exothermic tail gas combustion into a coupled micro-structured heat-exchanger reactor. The presented system has a power equivalent of 50 kWe and is intended to supply hydrogen filling stations with high-purity hydrogen in the future. To study the corresponding hydrogen production process, we use computer simulations on multiple scales. We use detailed computational fluid dynamics (CFD) simulations to simulate the chemically reactive flow in both a representative elementary volume and the entire integrated reactor. CFD simulations for ammonia decomposition in micro-structured reactors have already been investigated, e.g., in the review paper by Ao et al. [19] and the references therein. We then use the process simulation software ProSimPlus® to model the overall process and evaluate its performance. Due to the complexity of the integrated reactor, standard simulation modules from process simulators are not sufficient for accurately describing the reactors behavior. Therefore, we develop a multi-scale process simulation model that integrates a surrogate model derived from the CFD models. The potential of combining multiple simulation scales for process simulation has already been studied in [20–22], where it was shown that this approach leads to improved simulation results. In the present work, we present a flexible approach to couple a surrogate model derived from the detailed simulation models with ProSimPlus®. Finally, we use this model to evaluate the novel integrated reactor and show its benefits over alternative approaches.

2 Methods and Models

In this section, the integrated reactor concept for ammonia decomposition is presented together with the mathematical multi-scale model of the reactor and corresponding process.

2.1 Presentation of an Integrated Reactor Concept

The main objective for the development described in this paper is the production of hydrogen with suitable purity for PEM fuel cells [23] by catalytic decomposition of ammonia according to

$$2\mathrm{NH_3} \leftrightarrows \mathrm{N_2} + 3\mathrm{H_2} \quad \Delta_R H = +45.9\ \mathrm{kJ\ mol^{-1}}, \tag{1}$$

at an energetic efficiency as high as possible. Consequently, this work focuses on the choice of the appropriate purification device and the design of the ammonia decomposition reactor as the two main components. A low-temperature PEM fuel cell has been chosen as the hydrogen consumption device to demonstrate the high purity of the generated hydrogen at a power equivalent of 50 kWe based on lower heating values.

Under technical relevant process conditions of the coated homemade Ni-based catalyst, traces of ammonia between 333 ppm and 3409 ppm (650°C at 1 atm and 700°C at 15 bar, respectively) are to be expected in the cracked gas at thermodynamic equilibrium. Considering the potential to produce high purity hydrogen with an ammonia content of < 100 ppb(molar) at high pressure, which reduces the power demand for hydrogen compression at the filling station, pressure swing adsorption (PSA) is regarded as the best suited purification technology for the current application. The highly caloric tail gas released from the adsorbents upon depressurization can be utilized in the process as heat source to achieve a high process efficiency.

For the application of fuel reforming, Petrachi et al. [24] and Kolb et al. [25] demonstrated that internal heating by integrated combustion is far more efficient than heating with hot gas produced by an external burner. Because ammonia decomposition is – similar to steam reforming of fuels – an endothermic reaction and combustible gas is available from the off-gas outlet of the PSA unit, the ammonia cracking reactor can be equipped with an integrated catalytic burner to supply thermal power to the cracking reaction. The hydrogen and ammonia fuels contained in the PSA tail gas generate heat at the catalyst surface when reacting with oxygen of ambient air according to the following formulas:

$$2\mathrm{H_2} + \mathrm{O_2} \rightarrow 2\mathrm{H_2O} \quad \Delta_R H = -241.8\ \mathrm{kJ\ mol^{-1}}, \tag{2}$$

$$4\mathrm{NH_3} + 3\mathrm{O_2} \rightarrow 2\mathrm{N_2} + 6\mathrm{H_2O} \quad \Delta_R H = -633.7\ \mathrm{kJ\ mol^{-1}}. \tag{3}$$

Besides heat and the main reaction products, water and nitrogen, nitrogen oxides NO_x and nitrous oxide N_2O are formed as by-products at high temperatures and excess oxygen according to the following formulas:

$$4\mathrm{NH_3} + 5\mathrm{O_2} \rightarrow 4\mathrm{NO} + 6\mathrm{H_2O} \quad \Delta_R H = -906.3\ \mathrm{kJ\ mol^{-1}}, \tag{4}$$

$$4\mathrm{NH_3} + 7\mathrm{O_2} \rightarrow 4\mathrm{NO_2} + 6\mathrm{H_2O} \quad \Delta_R H = -1134.6\ \mathrm{kJ\ mol^{-1}}, \tag{5}$$

$$4\mathrm{NH_3} + 4\mathrm{O_2} \rightarrow 2\mathrm{N_2O} + 6\mathrm{H_2O} \quad \Delta_R H = -1103.2\ \mathrm{kJ\ mol^{-1}}. \tag{6}$$

To realize the thermal coupling of reaction , (1) with reactions (2) and (3), the integrated reactor is fabricated as a stack of catalyst-coated micro-structured stainless-steel foils with manifolds for fluid connections as well as top and bottom plates for stability by laser welding. Parallel microchannels coated with homemade Ni-based catalyst for reaction , (1) and Pt-based catalyst for reactions (2) and (3) are present on both sides of the foils on top of each other and the reaction heat flows through a thin metal slab between those channels [25]. Experimentally derived weight hourly space velocities (WHSV) for the ammonia decomposition catalyst and the hydrogen combustion catalyst, which lead to equilibrium and full conversion of ammonia and hydrogen, respectively, determine the amount of catalyst that needs to be present in both types of microchannels for the desired output level of the set-up. Throughout the rest of this paper, we denote by DEC (for ammonia decomposition) the part of the reactor where the endothermic ammonia decomposition takes place, and by AFB (for adiabatic fuel burning) the part of the reactor where the exothermic tail gas combustion takes place. The final reactor is manufactured by stacking pairs of DEC and AFB layers and consists of 72 pairs of layers. Each DEC layer has 210 channels with an elliptic cross section of 500 µm diameter, 600 µm height, and a length of

215 mm. Each AFB layer has 120 channels with a circular cross section of 500 µm radius and a length of 215 mm. This setup is shown in Figure 1.

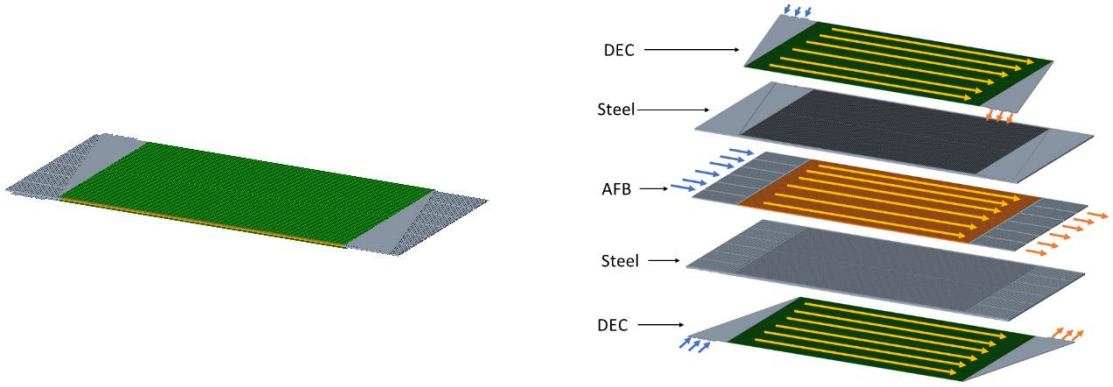

Figure 1. Geometry of the integrated reactor. Left: Compact view of the reactor. Right: Exploded assembly drawing of the geometries, including the steel part, the part of the reactor where the ammonia decomposition takes place (DEC), and the part where the tail gas combustion takes place (AFB).

The complete ammonia cracking system consists of the integrated reactor and the PSA unit, where the hydrogen in the cracked gas is separated from nitrogen. To establish optimum operating conditions for these two apparatuses, additional balance-of-plant components, such as heat exchangers, evaporators, and pressure changers are required. Figure 2 shows a simplified flow scheme of the proposed ammonia cracking process.

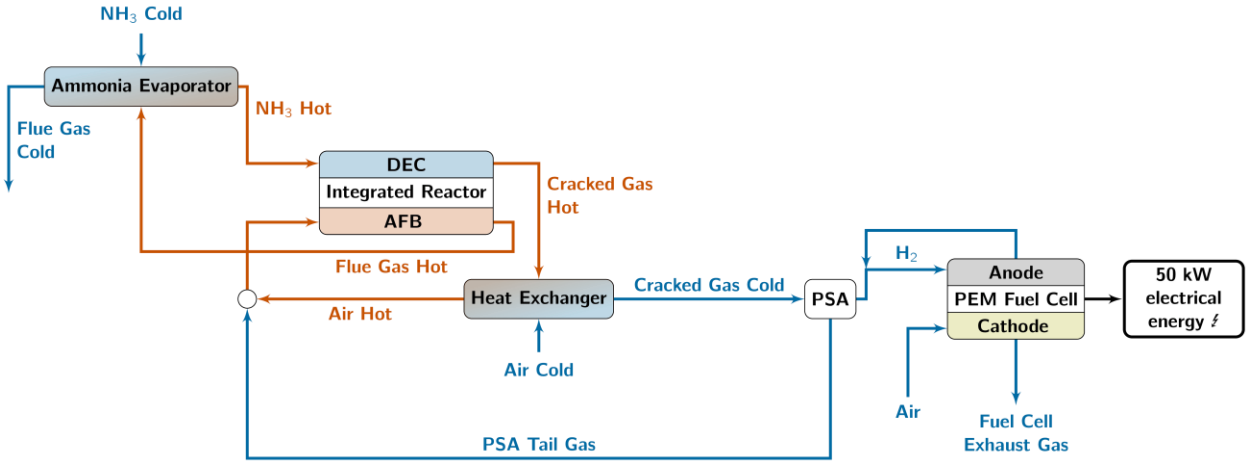

Figure 2. Simplified flowsheet of the ammonia cracking process.

2.2 Mathematical Model of Chemically Reacting Flow

To model the microchannel reactor shown in Figure 1, we use a set of partial differential equations (PDEs) accounting for mass, momentum, and heat transfer, as well as chemical reactions in the reactor. In the following, we give a brief presentation of our model; a detailed description can be found, e.g., in [19, 26, 27]. We use the following notations: The domain of the reactor is denoted by Ω, which consists of the domain of the AFB part Ω_{AFB}, the domain of the DEC part Ω_{DEC}, and the steel walls Ω_{steel} into which these geometries are etched. For simplicity, the fluid domain is defined as $\Omega_{\mathrm{fluid}} = \Omega_{\mathrm{AFB}} \cup \Omega_{\mathrm{DEC}}$. The boundary of Ω is denoted by $\Gamma = \partial\Omega$ and is divided into the inlets of the reactors Γ_{in}, the outer boundary Γ_{wall}, the symmetry boundary Γ_{sym}, and the outlets of the reactors Γ_{out}. Additionally, we have the interface between the reactors and the steel $\Gamma_{\mathrm{int}} = \partial\Omega_{\mathrm{fluid}} \setminus \partial\Omega$.

We assume steady and laminar flow. Therefore, the conservation of mass and momentum are given by

$$\nabla \cdot (\rho u) = 0 \quad \text{in } \Omega_{\text{fluid}},$$

$$\rho(u \cdot \nabla)u + \nabla p - \mu \Delta u - \frac{\mu}{3}\nabla(\nabla \cdot u) + S_u = 0 \quad \text{in } \Omega_{\text{fluid}}. \tag{7}$$

Here, u and p are the gases velocity and pressure, μ is the dynamic viscosity, and ρ denotes the density. The term S_u denotes an additional momentum source or sink, which is, e.g., needed when porous media are considered.

The conservation of chemical species k is described using their mass fraction Y_k

$$\rho\left(\frac{\partial Y_k}{\partial t} + u \cdot \nabla Y_k\right) + \nabla \cdot (\rho V^c Y_k) - \nabla \cdot \left(\rho D_{k,\text{mix}} \nabla Y_k\right) \quad = \quad \dot{\omega}_k \qquad \text{in } (0, t_{\max}) \times \Omega_{\text{fluid}}. \tag{8}$$

Here, a so-called correction velocity V^c (cf. [27]) is used, which ensures the consistency of the model. Moreover, $D_{k,\text{mix}}$ is the mixture-averaged diffusion coefficient of species k and $t_{\max}$ is the time horizon of the PDE. The species interact with each other in form of a reversible chemical reaction of the general form

$$\sum_k \nu'_k \mathcal{M}_k \leftrightarrows \sum_k \nu''_k \mathcal{M}_k, \tag{9}$$

where ν'_k and ν''_k are the (non-negative) stoichiometric coefficients of species k in the forward and reverse direction of the reaction, respectively. Species k is denoted by $\mathcal{M}_k$. The source term $\dot{\omega}_k$ due to the chemical reaction is given by

$$\dot{\omega}_k = M_k \nu_k Q, \tag{10}$$

where M_k is the molar mass of species k, $\nu_k = \nu''_k - \nu'_k$, and Q is the reaction rate given by

$$Q = k_f \left(\left(\prod_k [X_k]^{\nu'_k} \right)^{m_{\text{emp}}} - \left(\frac{\prod_k [X_k]^{\nu''_k}}{k_{\text{eq}}} \right)^{m_{\text{emp}}} \right). \tag{11}$$

Here, $[X_k]$ denotes the molar concentration of species k, k_{eq} is the equilibrium constant of the reaction, and m_{emp} is an empirical exponent used to model a non-integer reaction order. This rate equation is used, e.g., in [27–29] to model the reaction rate in the Sabatier process and is equivalent to the usual reaction rate for $m_{\text{emp}} = 1$. Note that Eq. (11) is an approximation of the reaction rate. For more details on its modeling, see e.g. [30]. For the forward reaction coefficient k_f, we use the usual Arrhenius model

$$k_f = A \exp\left(-\frac{E_a}{RT}\right), \tag{12}$$

where A is the pre-exponential factor, E_a the activation energy, R the universal gas constant, and T the temperature.

The conservation of energy is formulated via

$$\rho C_p \left(\frac{\partial T}{\partial t} + u \cdot \nabla T\right) - \nabla \cdot (\kappa \nabla T) \quad = \quad \dot{\omega}_T \qquad \text{in } (0, t_{\max}) \times \Omega. \tag{13}$$

Here, C_p is the specific heat capacity and κ the thermal conductivity. A heat source term, which will be specified in the following sections, is denoted by $\dot{\omega}_T$. Note that the above equation also holds in Ω_{steel} by setting $u = 0$. The transport parameters μ, ρ, C_p, and κ depend on the material considered in the respective part of the reactor and additionally on the temperature, unless otherwise specified.

For the sake of brevity, the boundary conditions for the PDE systems are specified in the supporting information.

The mathematical model presented above is used in the following sections to model the chemically reacting flow inside the reactor. In each section, it is adjusted to the desired level of detail. For more details, we refer to previous works [26, 27], where similar models are described.

2.3 Detailed Reactor Simulation

For the construction of the entire reactor, it is essential to gain insights into the processes in a single channel. Moreover, such a description can give important information for simulations on a larger scale. We assume that we can extract a small symmetric section from the geometry consisting of only one fourth of the respective channels, which is similar to [31]. Note that, to do so, the dimensions and the cross sections of the channels are slightly modified.

The flow in the channels is assumed to be laminar and fully developed (cf. [6]). Due to computational simplifications (recomputation of flow), we also consider the flow as incompressible. However, the channels are thermally coupled, and the heat transfer inside the plate material has to be taken into account. Due to the small excerpt, it is possible to resolve the catalyst layer as isotropic porous material. Therefore, an additional porous domain Ω_{cat} at the walls of the channels is introduced. It is assumed that reactions only proceed there and not in the gas phase. In this domain, the source term S_u is defined as $S_u = \mu K^{-1} u$, where K is the permeability of the catalyst layer.

The transport of species and the evolution of temperature in this section are modeled using Eqs. (7), 8), and (13) with the simplification $V^C = 0$. The parameters for the reaction kinetics in Eq. (12) are taken from [6] for the ammonia decomposition reaction and from [32] for the hydrogen combustion reaction. As stated in [6], only the forward reaction for ammonia decomposition is considered since the equilibrium constant is very large. Note that the kinetics identified in the supporting information cannot be used here since other assumptions are made. The heat source term in the catalyst layer is modeled as in [27].

To compute the steady flow fields in the two channels, the open-source software OpenFOAM® [33], version 8, is used. The evolution of temperature and concentration is simulated with the software tool PoreChem [34], which is developed at Fraunhofer ITWM. Here, it is assumed that the material properties are independent of temperature.

2.4 Thermal Reactor Simulation

While being very detailed and accurate, the model presented in the previous section is not suited for simulating the reactor in a larger scope due to the prohibitive numerical costs. Therefore, in this section, we present a thermal CFD model, which we use to simulate a representative layer of the reactor consisting of several hundred microchannels.

Our setting is as follows: We consider a representative periodic section of the reactor, consisting of one layer of the AFB part in the middle surrounded by two half-layers of the DEC part above and below, respectively. Additionally, we do not take into account boundary effects, but model the reactor as completely periodic, allowing us to simulate only the three representative layers mentioned above (cf. Figure 1).

In contrast to the previously described model, we consider only the thermal effects of the reactions as follows: We assume that the reactions proceed to completion / equilibrium and use the model of Section 2.3 to estimate the length L_{reac} required by the reactions to do so. We compute the corresponding heat of the reactions, which are used to define a suitable heat source term for the temperature equation. The heat source is then only active in the initial part of the microchannels before the gases reach a distance greater than L_{reac}. For simplicity, we assume that the heat is distributed evenly so that the resulting heat source is piecewise constant, i.e.,

$$\dot{\omega}_T(x) = \begin{cases} \dot{\omega}_{\mathrm{T,AFB}} & \text{if } x \in \Omega_{\mathrm{AFB,\,reac}}, \\ \dot{\omega}_{\mathrm{T,DEC}} & \text{if } x \in \Omega_{\mathrm{DEC,\,reac}}, \\ 0 & \text{else.} \end{cases} \tag{14}$$

Here, $\Omega_{\mathrm{AFB,\,reac}}$ and $\Omega_{\mathrm{DEC,\,reac}}$ denote the “reactive part” of the AFB and DEC microchannels, which is determined by the detailed CFD model from Section 2.3. We also assume that the transport properties of the gases do not change due to the reaction, which allows us to model the flow as incompressible due

to the low gas velocity in each microchannel. Of course, for this thermal model, we drop the species conservation equation 8) as we do not model the chemical reactions explicitly.

We solve the presented model with Ansys® Fluent, 2022 R2 [35]. The corresponding results are discussed in Section 3.2. There, we observe large temperature differences between the channels, particularly at the beginning of the microchannels.

Current process simulation software are not able to describe such temperature differences, so it is usually assumed that all channels have the same temperature. To overcome this limitation, in the next section we present a surrogate model that incorporates the temperature distribution computed with the thermal CFD model and can be used within a process simulation software.

2.5 Hybrid Process Simulation

2.5.1 Surrogate Model for the Integrated Reactor

With the models from Sections 2.3 and 2.4, we have a spatially resolved temperature distribution inside the reactor. From this, we derive a fast surrogate model in the form of a Python module, which we then use in the process simulation.

For this surrogate model, we divide a single layer of the reactor into N_c different groups of channels. For each, we extract a representative temperature distribution from the thermal model. We then model each group independently by a single plug flow reactor with a given temperature profile. Hence, we proceed analogously to [27] and only simulate the fluid velocity, pressure, and species mass fractions with this surrogate model for each of the $2N_\mathrm{c}$ one-dimensional plug flow reactors. In the end, all outputs are mixed to obtain a single output stream. This procedure simplifies the numerical effort substantially.

For the ammonia decomposition reaction, we use the reaction kinetics identified in the supporting information for simulating the reaction , (1). As the catalytic combustion of hydrogen proceeds very rapidly, we use a different model for this reaction: As we assume that the reaction takes place over the length L_reac of the channel (cf. Section 2.4), we compute the chemical equilibrium of the reaction system (2)–(6) for the temperature obtained at this location and assume that it is reached. This approach allows us to qualitatively study the formation of nitrogen oxides NO_x resulting from the combustion of ammonia.

For the simulation of the plug flow reactors, we use the finite element package FEniCS [36]. For more details, particularly regarding the implementation of the temperature-dependent transport properties of the gases, we refer to [26, 27] and the references therein.

2.5.2 Process Simulation in ProSimPlus®

To model the complete process around the integrated reactor, including the hydrogen separation step and the fuel cell, we use the process simulation software ProSimPlus® [37]. In ProSimPlus®, the process simulation is based on a sequential modular approach. The process is modeled using single modules, which are connected by material and information streams.

The process consists of three main elements: the integrated reactor used for ammonia decomposition, the PSA unit used for hydrogen separation, and the fuel cell. The fuel cell is modeled using a component splitter for the anode and a Gibbs reactor for the cathode. The PSA unit is modeled using a component splitter with specified recovery ratio for hydrogen and nitrogen. Modeling the integrated reactor is a more complicated task. As explained before, ammonia decomposition and tail gas combustion occur in layers of alternatingly stacked channels in the reactor, the exothermic tail gas combustion reactions providing the required heat for the endothermic ammonia decomposition reaction. As shown later in Section 3.2, this leads to a complex temperature distribution in the reactor, which cannot be represented with standard simulation modules. Therefore, the integrated reactor is modeled using a custom module programmed in a so-called Windows Script. This custom module handles the communication with the Python-based surrogate model presented in Section 2.5.1. The module has two

feed streams: the ammonia feed and the mixture of the PSA tail gas with air. Its outlet streams are the cracked gas from ammonia decomposition and the flue gas from tail gas combustion. As shown in Figure 2, the ammonia feed is pre-heated before entering the reactor. The required heat duty is obtained by cooling the hot flue gas. In the process simulation, the heating and cooling steps are separately modeled by heat exchangers, which are connected through their heat duty. Also, the cracked gas is cooled down before entering the PSA. Here, air is used as cooling fluid. The pre-heated air is then mixed with the tail gas from the PSA and used for combustion.

In the next section, we present the custom module for the reactor simulation in more detail.

2.5.3 Coupling of CFD Model and Process Simulation Software

As explained before, in the process simulation, we use the surrogate model presented in Section 2.5.1 instead of standard simulation modules to simulate the integrated reactor. To do this, we need to connect the surrogate model to ProSimPlus® [37].

Because the surrogate model is solved with FEniCS, it can only run natively on Linux or MacOS, whereas ProSimPlus® runs on Windows. Therefore, we need to ensure that we can use the surrogate model on a Windows platform as well. To do so, we use the software Podman [38], which allows us to package the Python-based simulation model in a so-called container, a stand-alone and isolated unit of software that contains the surrogate model and its dependencies. The container can then be run on Windows systems. In fact, we use the Windows Subsystem for Linux (WSL) to run a Ubuntu Linux distribution and start the container.

To use the surrogate model within the process simulation, we use a so-called Windows Script module in ProSimPlus® to create a custom module inside the flowsheet. When this custom module is computed, the information on the module's feed streams is written to a text file, which is processed by the surrogate model in the container. Then, the custom module starts the container via the WSL. Once the surrogate model has been solved for the given feed streams, the outlet streams are written to another text file and this information is processed in the custom module in ProSimPlus®. The overall modeling and simulation procedure is visualized in Figure 3.

The approach using a container in a custom module of the flowsheet simulation for packaging the surrogate model is very flexible – in principle it allows us to replace any module of the flowsheet with arbitrarily complex simulation models.

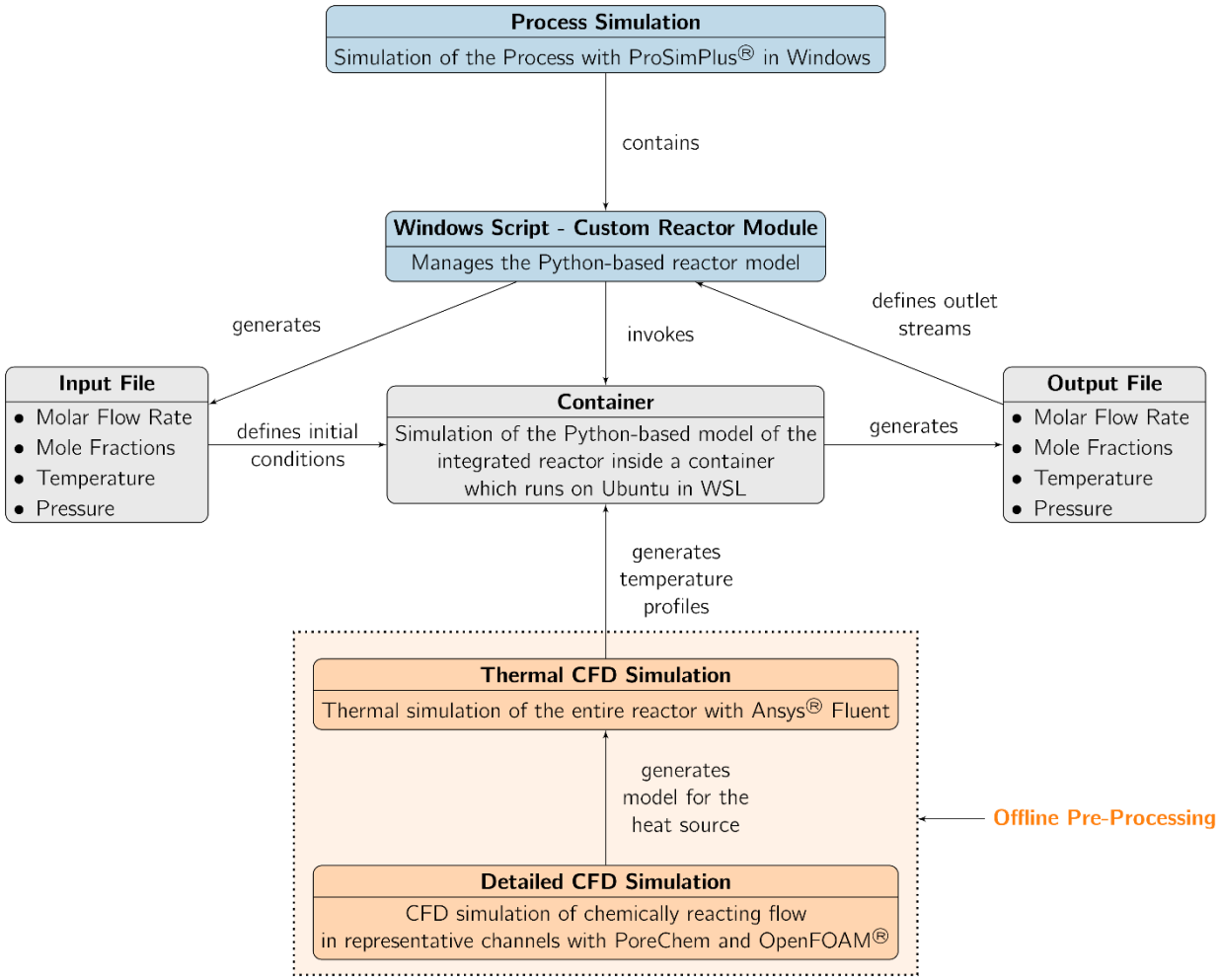

Figure 3. Overview of the coupling between the process simulation software ProSimPlus® and the Python-based reactor model. The process simulation software is colored blue, the CFD simulations are colored in orange, and our custom modules are colored in gray.

3 Results and Discussion

In Section 2, we have introduced a new integrated reactor concept and corresponding process for hydrogen production from ammonia decomposition. We have presented our approach for modeling and simulating the process based on a combination of multiple scales, namely, a detailed CFD simulation of a portion of the reactor, a thermal simulation of the entire reactor, and a complete process simulation. In this section, we show the results of the different modeling scales and demonstrate the potential of the introduced reactor concept.

3.1 Estimation of the Length of the Reactive Zone

With the detailed simulation of a section of the reactor, the consumption of the reactants can be investigated. This can give an idea about the length of the reactive zone L_{reac} and the production of heat.

Simulations of the full system of equations showed that a steady-state temperature profile is reached after some time. For different lengths of the small excerpt, the mean concentrations in the respective channel cross sections are shown in Figure 4. The longest excerpt has a length of 16 mm. A prediction of the further decline of the concentration is estimated using exponential regression, i.e., a linear regression on the logarithm of the data.

Since the exponential regression never reaches zero, we choose a cut-off value of 1e-2 and get for the AFB part approximately 57 mm. Note that for the DEC part, this value is reached around 25 mm. As shown in Figure S3 in the supporting information, the convective transport in the AFB channel is nonuniform. This might lead to even faster or slower decline in both parts. Moreover, as stated before, only the forward reaction is considered in the DEC part. An equilibrium reaction might lead to a slightly higher concentration in this part. Therefore, we choose the larger length of the presented results and set L_{reac} to be 25% of the length of the channels, i.e., 53.75 mm.

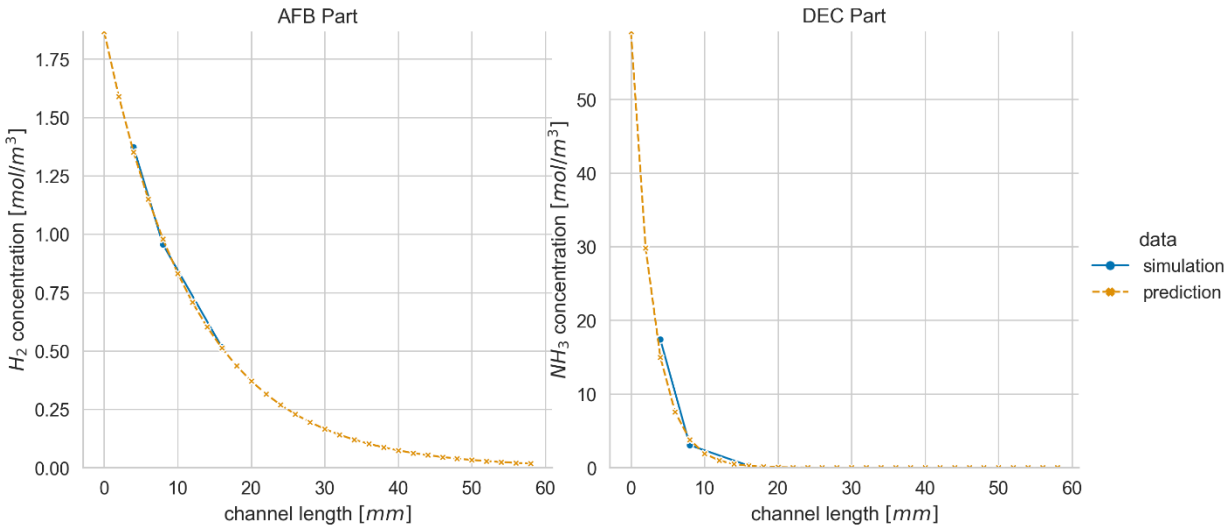

Figure 4. Concentration profiles inside the different parts of the reactor. Concentration of H_2 in the AFB part (left), and concentration of NH_3 in the DEC part (right), and prediction of the concentration decline for estimating the reaction length.

3.2 Temperature Distribution Inside the Reactor

Let us now investigate the thermal reactor simulation with the model presented in Section 2.4. The flow characteristics of the reactor are provided in the supporting information. The results presented there justify the assumption in Section 2.5, where we assume to have a uniform flow distribution among the channels.

The temperature distribution in the reactor is shown in Figure 5. There the temperature is shown in a plane parallel to and in-between the reaction channels. We observe the following: As the inlet temperature for the gas in the AFB part is comparatively low (around 365 °C) and the inlet temperature for the DEC part is comparatively high (around 650 °C), we see large temperature gradients near the inlet. This is because the flow enters the AFB part from the top (from the angle of view in Figure 5), whereas it enters the DEC part from the left and right sides, alternating between layers, cf. Figure 1. This is done to ensure a symmetric temperature distribution in the reactor. At the start of the microchannels, there is a steep temperature rise in flow direction (from top to bottom), which is due to the heat source term modeling the influence of the chemical reactions. After a quarter of the channel length, i.e., after the length L_{reac}, the heat source term vanishes. Over the remaining length of the channels, temperature differences are smoothed out due to thermal conduction.

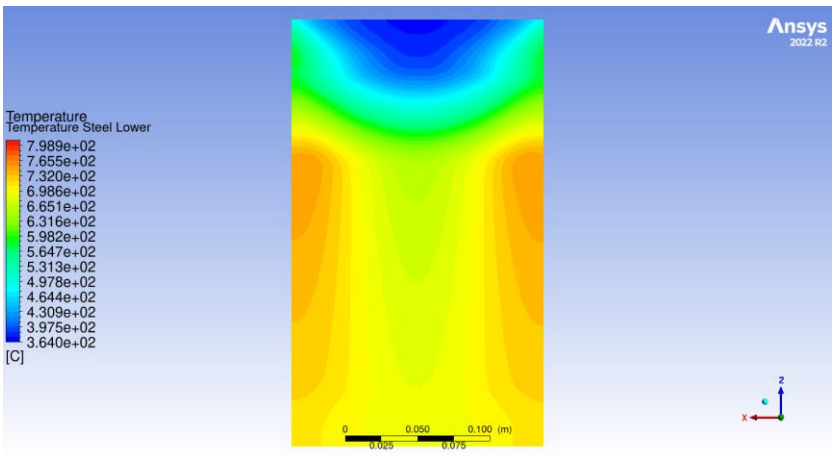

Figure 5. Temperature distribution in the reactor.

These results are also confirmed in Figure 6 and Figure 7, where the temperature distribution across and along the channels, respectively, is shown. In Figure 6, we observe large temperature differences between the channels, particularly near the inlets, but there is not much difference between the temperatures in the DEC and AFB parts. Further downstream, in the middle of the plate length, there is still roughly a temperature difference of 100 °C between the middle and outer channels, which is further reduced due to thermal conduction near the outlet. In Figure 7, the temperature is shown along the channels for two outer and one middle channels. There, we observe similar trends: In the beginning, the heat source term is the dominant factor for the temperature, resulting in a steep temperature increase over the length L_{reac}. After that, we see a slow decrease of temperature for the left and right outer channels, whereas we see an increase of temperature for the middle one, which is due to the equilibrating effect of thermal conduction.

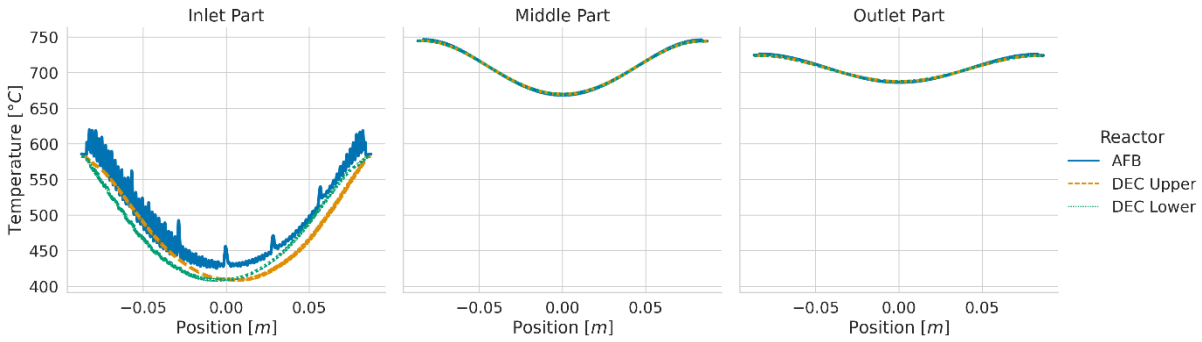

Figure 6. Temperature distribution at the inlet (left), middle (middle) and outlet (right) sections across the microchannels.

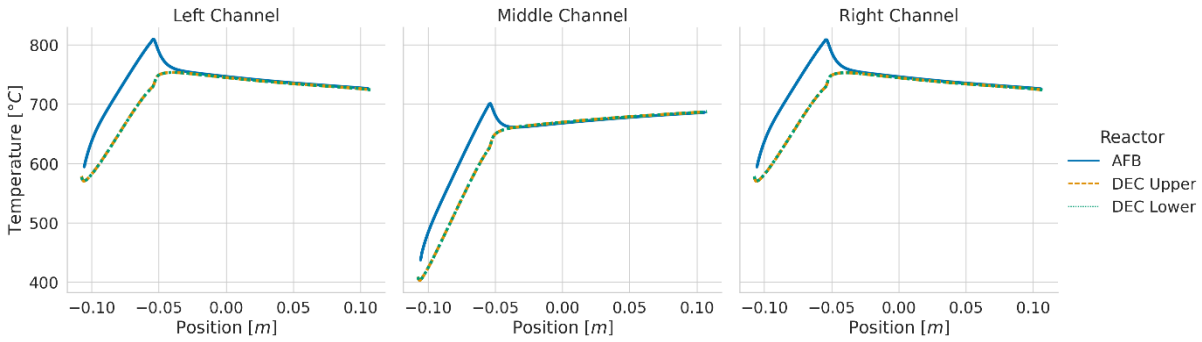

Figure 7. Evolution of the temperature along three representative channels.

3.3 Evaluation of the Ammonia Cracking System using Multi-Scale Modeling

As a last step, we simulate the overall process using the hybrid simulation setup presented in Section 2.5. Besides the reactions occurring in the integrated reactor, this includes a hydrogen separation step, recycling of the tail gas of the separation unit and generation of energy using a fuel cell. As explained before, we use the surrogate model presented in Section 2.5.1 with the temperature distribution presented in the previous section to compute the outlet streams of the reactor. These are further processed in the flowsheet simulation.

The results discussed below were obtained for the following settings: the ammonia feed has a mass flow rate of 21.13 kg/h and enters the process at 25.1°C and 10 bar in liquid state. It is then evaporated and heated up to 644.1°C before entering the reactor. The pressure in the DEC part of the reactor is 10 bar, while the AFB part of the reactor is operated at 1 atm. The recovery ratio for the PSA corresponds to a high operating pressure of 10 bar, which is the pressure of its feed stream. The PSA tail gas is released at a pressure of 1 atm, while the purified pressurized hydrogen is expanded from 10 to 2 bar before being fed to the fuel cell.

For these settings, an ammonia conversion of 99.6% is achieved. Accordingly, the cracked gas contains 0.4 wt.% remaining ammonia, 17.7 wt.% hydrogen, and 81.9 wt.% nitrogen. At 10 bar, 78% hydrogen and 1.2% nitrogen are recovered in the overhead product of the PSA. Accordingly, the tail gas contains 4.6 wt.% hydrogen, 94.9 wt.% nitrogen, and 0.5 wt.% ammonia for a total mass flow rate of 18.0 kg/h. The tail gas is then mixed with the 110 kg/h air used for cooling the cracked gas to supply oxygen for the combustion. This results in an air-fuel ratio of 3.8 in the mixed gas. Due to remaining ammonia in the tail gas, 23 mg/m^3 nitrogen oxides NO_x are formed during the combustion reaction.

The overhead product of the PSA, which contains almost pure hydrogen, is used for power generation in the fuel cell. In total, 2.9 kg/h hydrogen are available. To calculate the power generated by the fuel cell, we use the following equation:

$$P_{\mathrm{el,FP}} = \Delta_R H \cdot \frac{1}{\lambda_{\mathrm{A}}} \cdot \eta_{\mathrm{el,FC}} \cdot \dot{n}_{H_2}, \tag{15}$$

where $\Delta_R H$ is the enthalpy of reaction, λ_{A} the fuel excess ratio at the fuel cell anode, $\eta_{\mathrm{el,FC}}$ the electrical efficiency of the fuel cell, and $\dot{n}_{H_2}$ the molar flow rate of hydrogen. In our simulation, we assume that $\lambda_{\mathrm{A}} = 1.01$ and $\eta_{\mathrm{el,FC}} = 0.52$. The enthalpy of reaction amounts to -242.2 kJ/mol. According to Eq. (15), 50 kWe can be generated by the fuel cell with the available hydrogen. It should be noted that the process has been designed to meet this power requirement and the process parameters have been chosen accordingly.

To assess the efficiency of the presented process, we compute the fuel processor efficiency and the electrical efficiency. The fuel processor efficiency compares the power contained in the hydrogen produced by the fuel processor to the power contained in the ammonia used in the process and is defined as follows:

$$\eta_{\mathrm{FP}} = \frac{P_{\mathrm{H_2}}}{P_{\mathrm{NH_3}} + \sum_j \dot{Q}_{\mathrm{ext},j}} = \frac{\dot{n}_{\mathrm{H_2}} \cdot H_{i,\mathrm{H_2}}}{\dot{n}_{\mathrm{NH_3}} \cdot H_{i,\mathrm{NH_3}} + \sum_j \dot{Q}_{\mathrm{ext},j}}, \tag{16}$$

where $P_{\mathrm{H_2}}$ and $P_{\mathrm{NH_3}}$ are the power (or energy content) contained in the hydrogen and ammonia mass flows, respectively, $\dot{Q}_{\mathrm{ext},j}$ is the external heat duty required for each apparatus j of the fuel processor, if any, and H_i the lower heating value of each gas flow. The electrical efficiency of the entire process compares the power generated by the fuel cell to the power contained in the ammonia feed flow used in the process and is defined as follows:

$$\eta_{\mathrm{el,tot}} = \frac{P_{\mathrm{el,FP}}}{\dot{n}_{\mathrm{NH_3}} \cdot H_{i,\mathrm{NH_3}} + \sum_j \dot{Q}_{\mathrm{ext},j}}, \tag{17}$$

where $P_{\mathrm{el,FP}}$ is the electrical power generated by the fuel cell as calculated with Eq. (15).

In the process investigated in this paper, thermal coupling is used to provide the required heat duty for ammonia decomposition from hydrogen combustion. Therefore, no external heat source $\dot{Q}_{\mathrm{ext}}$ is required. Moreover, heat integration is used to heat and cool down the reactor feed and outlet streams, so there is also no need for an external power source. As a result, using Eqs. (16) and (17), we obtain a fuel processor efficiency η_{FP} of 88% and an electrical efficiency $\eta_{\mathrm{el,tot}}$ of 45.8%. This means that 88% of the energy contained in the ammonia used in the process is recovered in the hydrogen supplied by the process. The electrical efficiency shows that that the electrical power generated by the fuel cell with the provided hydrogen corresponds to 45.8% of the energy contained in the ammonia feed flow that could have been obtained by direct combustion of the ammonia.

In Table 1, a comparison of the novel ammonia cracking system to the systems mentioned in the introduction in terms of efficiency is given. As can be seen from this table, the presented concept shows superior efficiency than e-crackers [13, 14] and some of the systems using anode off-gas from PEM fuel cells [16, 18]. Only the ZBT cracker [17] reaches better efficiencies. However, high efficiencies can only be achieved by combustion of the anode off-gas of a PEM fuel cell in this case, the presence of which is then mandatory. The integrated reactor concept presented in this paper can be used independently of a fuel cell to supply high purity hydrogen, e.g., to hydrogen filling stations.

Table 1. Comparison of different ammonia cracking systems in terms of efficiency.

Heat source	Fuel processor efficiency [a)]	Electrical efficiency [b)]	Reference [c)]
PSA tail gas	88.0%	45.8%	This work
Electrical	77.4%	n.a. [d)]	[13]
Electrical	73.6%	40.5%	[14]
Anode off-gas	68.8%	35.8%	[16]
Anode off-gas	114.5%	57.0%	[17]
Anode off-gas	n.a. [d)]	31.0%	[18]

a) Cf. Eq. (16); b) Cf. Eq. (17); c) Also refer to SI for more details on the numbers; d) not available.

The main advantage of the presented integrated reactor concept is the possibility to cover the entire energy demand for the endothermic ammonia decomposition reaction by combustion of residual hydrogen from the separation step. Thus, not only is energy saved, but also waste from the process is avoided through its direct use in the process itself. In fact, 20 kW of heat supply are required for ammonia decomposition. Without thermal coupling, this energy would have to be provided externally, e.g., through electric heating. Moreover, without the hot gas flow originating from hydrogen combustion, pre-heating the ammonia feed would also require 17 kW of electric energy. The effect on the efficiencies can be calculated by adding these two external heat sources $\dot{Q}_{\mathrm{ext},j}$ to the enumerator of both ratios as defined in Eqs. (16) and (17). This leads to a fuel processor efficiency of 65.7% and an electrical efficiency of 34.2%. These numbers show that an electrically heated system would be much less efficient than the new process based on an integrated reactor presented in Section 2.1. Thanks to the thermal coupling of ammonia decomposition and combustion of the hydrogen and remaining ammonia contained in the PSA off-gas, it is possible to improve the electrical efficiency by 11.6 percentage points and the fuel processor efficiency by 22.3 percentage points.

4 Conclusions and Outlook

In this paper, we have introduced a novel concept for hydrogen production by ammonia decomposition. The novel ammonia cracking system utilizes the tail gas of the pressure swing adsorption (PSA) system downstream, which is used for hydrogen separation, to supply the cracking reaction with energy. The

endothermic ammonia decomposition and exothermic tail gas combustion are thermally coupled in a micro-structured integrated reactor, which makes an external heat source obsolete.

To study the new hydrogen production process, we have developed an appropriate simulation model. It combines multiple scales to accurately describe the phenomena at different levels in the process. It consists of a detailed CFD model for the reaction inside the microchannels, a thermal reactor model for the entire integrated reactor, and a model for the entire process in a process simulation software. The different CFD models are combined in a fast surrogate model that is used within the process simulation. We have proposed a coupling strategy for integrating the CFD-based models into the process simulation software with the help of a so-called container. This coupling enables the incorporation of arbitrarily complex simulation models into the process simulation with the potential of significantly enhancing and improving the latter. Additionally, it allows for great flexibility in modeling certain parts of the process, where standard simulation modules have their shortcomings.

The numerical results have shown that the multi-scale model allows for a detailed simulation of the presented integrated reactor concept. They have also highlighted the potential of the new concept for hydrogen production from ammonia. The ammonia cracking system has a power equivalent of 50 kWe, corresponding to an output of 70 kg hydrogen per day. Thanks to thermal coupling between the ammonia decomposition reaction and the tail gas combustion reactions, as well as the absence of an external power source, high fuel processor and electrical efficiencies are obtained. These are comparable to the efficiencies of alternative processes for hydrogen generation using fuel combustion as heat source.

The ammonia cracking plant, the first prototype of which is currently being assembled and put into operation at Fraunhofer Institute for Microengineering and Microsystems IMM in Germany, is, among other applications, intended to supply hydrogen filling stations with high-purity hydrogen suitable for PEM fuel cells. In this contribution, we have limited the scope to one defined setting of the process parameters. The optimization of the process to maximize the efficiencies or minimize the NO_x emissions will be future work. Since these objectives are likely to be conflicting, multi-criteria optimization methods would be required. Moreover, the models used in this paper will be calibrated with experimental data from the prototype, e.g., from the PSA.

Supporting Information

Supporting Information for this article can be found under [Link provided by Wiley]. This section includes additional references to primary literature relevant for this research [39].

Acknowledgment

Financial support for project AMMONPAKTOR was provided by the EFRE program of the German region Rhineland-Palatinate under grant no. 84009390.

Symbols used

A	$\left[\frac{1}{s}\left(\frac{mol}{m^3}\right)^{1-m_{\mathrm{emp}}\sum_k \nu'_k}\right]$	pre-exponential factor
C_p	[J/kg/K]	specific heat capacity
$D_{k,\mathrm{mix}}$	[m^2/s]	mixture-averaged diffusion coefficient for species k
E_a	[J/mol]	activation energy

H_i	[J/mol]	lower heating value
$\Delta_R H$	[kJ/mol]	enthalpy of reaction
K	[m²]	permeability of the porous catalyst layer
k_{eq}	$\left[\left(\frac{mol}{m^3}\right)^{\sum_k \nu_k}\right]$	equilibrium constant of the reaction
k_f	$\left[\frac{1}{s}\left(\frac{mol}{m^3}\right)^{1-m_{\mathrm{emp}}\sum_k \nu'_k}\right]$	forward reaction coefficient
L_{reac}	[m]	length required for the reactions to proceed to completion
m_{emp}	[-]	empirical exponent for the reaction rate
$\mathcal{M}_k$	[]	symbol for species k
M_k	[kg/mol]	molar mass of species k
n	[-]	outward unit normal vector on Γ
$\dot{n}$	[mol/s]	molar flow rate
N_{c}	[-]	number of representative channels for the surrogate model
p	[Pa]	fluid pressure
P_{el}	[We]	electrical power
$P_{\mathrm{H_2}}$	[W]	power contained in the hydrogen mass flow
$P_{\mathrm{NH_3}}$	[W]	power contained in the ammonia mass flow
Q	[mol/m³/s]	rate of progress of the chemical reaction
R	[J/mol/K]	universal gas constant
S_u	[kg/m²/s²]	source term for the velocity in porous media
T	[K]	temperature
$t_{\max}$	[s]	time horizon of the PDEs
u	[m/s]	fluid velocity
u_c	[]	vector of control variables, $u_c = [\log(A), E_a, n]^T$
V_c	[m/s]	correction velocity
$[X_k]$	[mol/m³]	molar concentration of species k
y	[]	vector of state variables, $y = [p, u, Y^{\mathrm{vec}}]^T$
Y	[-]	vector of species mass fractions, $Y = [Y_1, \ldots, Y_m]^T$
Y_k	[-]	mass fraction of species k

Greek letters

Γ	[-]	boundary of the domain Ω
η	[-]	efficiency
κ	[W/m/K]	thermal conductivity
λ_A	[-]	fuel excess ratio at the anode of the fuel cell
μ	[Pa*s]	dynamic viscosity

ν_k	[-]	difference of stoichiometric coefficients for species k
ν'_k	[-]	stoichiometric coefficient of species k in the forward direction of reaction
ν''_k	[-]	stoichiometric coefficient of species k in the reverse direction of reaction
ρ	[kg/m³]	density
χ^{NH_3}	[-]	ammonia conversion
$\dot{\omega}_k$	[kg/m³/s]	reaction source term for species k
$\dot{\omega}_T$	[W/m³]	heat source term
Ω	[]	(computational) domain of the system of partial differential equations

Sub- and Superscripts

0	Initial conditions
cat	catalyst
el	electrical
emp	empirical
exp	experimental, measured
FC	fuel cell
FP	fuel processor
in	inlet
int	interface between fluid and steel
out	outlet
reac	reactive part of the DEC or AFB channels in the thermal reactor model
sim	simulated
sym	symmetry boundary
tot	total (entire process)

Abbreviations

AFB – hydrogen combustion (adiabatic fuel burning) part of the integrated reactor

BFGS method – Quasi-Newton method of Broyden, Fletcher, Goldfarb, and Shanno

CFD – computational fluid dynamics

DEC – ammonia decomposition part of the integrated reactor

PDE – partial differential equation

PSA – pressure swing adsorption

SI – supporting information

WHSV – weighted hourly space velocity

WSL – Windows Subsystem for Linux

References

[1] A. Mikhaylov, N. Moiseev, K. Aleshin, T. Burkhardt, *Entrepreneurship and Sustainability Issues* **2020**, *7 (4)*, 2897 – 2913. DOI: https://doi.org/10.9770/jesi.2020.7.4(21)

[2] https://www.umweltbundesamt.de/daten/klima/atmosphaerische-treibhausgas-konzentrationen (Accessed on September 05, 2023).

[3] H. Schüle, *Stromproduktion und Stromverbrauch im Jahre 2022 in der Bundesrepublik Deutschland: Auswertung von Daten der Bundesnetzagentur im Hinblick auf die Erzeugung von erneuerbarem Wind- und Solarstrom*, Neunburg vorm Wald **2023**.

[4] Kawasaki Heavy Industries, Ltd., *Liquefied Hydrogen Carrier -SUISO FRONTIER- Receives Classification from Nippon Kaiji Kyokai*, Kōbe, Hyōgo, Japan **2021**.

[5] https://shipfc.eu/ (Accessed on September 05, 2023).

[6] S. Chiuta, R. C. Everson, H. W. Neomagus, D. G. Bessarabov, *Int. J. Hydrogen Energy* **2016**, *41 (6)*, 3774 – 3785. DOI: https://doi.org/10.1016/j.ijhydene.2015.12.130

[7] A. Takahashi, T. Fujitani, *J. Chem. Eng. Jpn.* **2016**, *49 (1)*, 22 – 28. DOI: https://doi.org/10.1252/jcej.14we431

[8] I. Lucentini, G. García Colli, C. D. Luzi, I. Serrano, O. M. Martínez, J. Llorca, *Applied Catalysis B: Environmental* **2021**, *286*, 119896. DOI: https://doi.org/10.1016/j.apcatb.2021.119896

[9] H. Maleki, M. Fulton, V. Bertola, *Chemical Engineering Journal* **2021**, *411*, 128595. DOI: https://doi.org/10.1016/j.cej.2021.128595

[10] DIN EN 17124:2019-07, *Wasserstoff als Kraftstoff - Produktfestlegung und Qualitätssicherung - Protonenaustauschmembran(PEM)-Brennstoffzellenanwendungen für Straßenfahrzeuge*, Beuth Verlag GmbH, Berlin **2019**.

[11] M. Yáñez, F. Relvas, A. Ortiz, D. Gorri, A. Mendes, I. Ortiz, *Sep. Purif. Technol.* **2020**, *240*, 116334. DOI: https://doi.org/10.1016/j.seppur.2019.116334

[12] D. S. Wong, M. Dolan, *CSIRO's Metal Membrane Technology (MMT) – Technical Update*, 5th APAC conference, Newcastle, Australia **2023**.

[13] http://www.james-hogg.com/ht1_cracker_datasheet.pdf (Accessed on September 05, 2023).

[14] R. Nielsen, *Topsoes Ammonia cracking technology – Delivering green Hydrogen* **2021**.

[15] https://www.ammoniaenergy.org/articles/siemens-energy-begins-work-on-commercial-cracker-prototype/ (Accessed on August 31, 2023).

[16] A. Perna, M. Minutillo, S. Di Micco, V. Cigolotti, A. Pianese, *E3S Web Conf.* **2020**, *197*, 5001. DOI: https://doi.org/10.1051/e3sconf/202019705001

[17] F. E. Nigbur, *Ammoniak-Cracker zur Brenngasversorgung von Brennstoffzellen*, Dissertation, Universität Duisburg-Essen.

[18] https://www.gencellenergy.com/our-products/gencell-a5/ (Accessed on September 05, 2023).

[19] R. Ao, R. Lu, G. Leng, Y. Zhu, F. Yan, Q. Yu, *Energies* **2023**, *16 (2)*, 921. DOI: https://doi.org/10.3390/en16020921

[20] S. E. Zitney, M. Syamlal, in *European Symposium on Computer Aided Process Engineering-12, 35th European Symposium of the Working Party on Computer Aided Process Engineering*, Elsevier **2002**.

[21] S. E. Zitney, *Comput. Chem. Eng.* **2010**, *34 (9)*, 1532 – 1542. DOI: https://doi.org/10.1016/j.compchemeng.2010.02.011

[22] Z. Jaworski, B. Zakrzewska, *Comput. Chem. Eng.* **2011**, *35 (3)*, 434 – 445. DOI: https://doi.org/10.1016/j.compchemeng.2010.05.009

[23] I. Staffell, D. Scamman, A. Velazquez Abad, P. Balcombe, P. E. Dodds, P. Ekins, N. Shah, K. R. Ward, *Energy Environ. Sci.* **2019**, *12 (2)*, 463 – 491. DOI: https://doi.org/10.1039/C8EE01157E

[24] G. A. Petrachi, G. Negro, S. Specchia, G. Saracco, P. L. Maffettone, V. Specchia, *Ind. Eng. Chem. Res.* **2005**, *44 (25)*, 9422 – 9430. DOI: https://doi.org/10.1021/ie050215n

[25] G. Kolb, *Chemical Engineering and Processing: Process Intensification* **2013**, *65*, 1 – 44. DOI: https://doi.org/10.1016/j.cep.2012.10.015

[26] S. Blauth, *Adjoint-Based Shape Optimization and Optimal Control with Applications to Microchannel Systems*, Dissertation, Technische Universität Kaiserslautern.

[27] S. Blauth, C. Leithäuser, R. Pinnau, *J. Eng. Math.* **2021**, *128 (1)*. DOI: https://doi.org/10.1007/s10665-021-10134-2

[28] P. J. Lunde, F. L. Kester, *J. Catal.* **1973**, *30 (3)*, 423 – 429. DOI: https://doi.org/10.1016/0021-9517(73)90159-0

[29] P. J. Lunde, F. L. Kester, *Ind. Eng. Chem. Process Des. Dev.* **1974**, *13 (1)*, 27 – 33. DOI: https://doi.org/10.1021/i260049a005

[30] M. Baerns, H. Hofmann, A. Renken, *Chemische Reaktionstechnik*, 3rd ed., Lehrbuch der technischen Chemie, Vol. 1, Wiley-VCH, Weinheim **2004**.

[31] K. Schumacher, N. Engelbrecht, R. C. Everson, M. Friedl, D. G. Bessarabov, *Int. J. Hydrogen Energy* **2019**, *44 (13)*, 6415 – 6426. DOI: https://doi.org/10.1016/j.ijhydene.2019.01.132

[32] Y. Zhang, Y. Liu, *Frontiers in Energy Research* **2017**, *5*. DOI: https://doi.org/10.3389/fenrg.2017.00031

[33] H. G. Weller, G. Tabor, H. Jasak, C. Fureby, *Comput. Phys.* **1998**, *12 (6)*, 620 – 631. DOI: https://doi.org/10.1063/1.168744

[34] P. Toktaliev, O. Iliev, *Proc. Appl. Math. Mech.* **2023**, *23 (1)*. DOI: https://doi.org/10.1002/pamm.202200327

[35] Ansys, *Ansys® Fluent 2022 R2* **2022**.

[36] M. Alnaes, J. Blechta, J. Hake, A. Johansson, B. Kehlet, A. Logg, C. Richardson, J. Ring, M. E. Rognes, G. N. Wells, *Archive of numerical software* **2015**, *3 (100)*, 9 – 23.

[37] ProSim, *ProSimPlus®* **2023**.

[38] Podman, *Podman* **2023**.

[39] S. Blauth, *SoftwareX* **2021**, *13*, 100646. DOI: https://doi.org/10.1016/j.softx.2020.100646

Supporting Information

Multi-Scale Simulation of a Novel Integrated Reactor for Hydrogen Production by Ammonia Decomposition

Dr. Sebastian Blauth, Dr.-Ing. Julie Damay*, Dr. Sebastian Osterroth, Dr. Christian Leithäuser, Christian Hofmann, Dr.-Ing. Gunther Kolb, Martin Wichert, Dr. Konrad Steiner, and Prof. Dr. Michael Bortz

Correspondence: julie.damay@itwm.fraunhofer.de, Fraunhofer Institute for Industrial Mathematics ITWM, Fraunhofer-Platz 1, 67663 Kaiserslautern, Germany

1 Methods and Models

1.1 Boundary Conditions

We use the following boundary conditions for our PDE system (Eqs. (7), (8), and (13) in the manuscript): At the inlet, Dirichlet conditions are specified

$$u = u_{\text{in}}, \qquad T = T_{\text{in}}, \qquad Y_k = Y_k^{\text{in}} \qquad \text{on } \Gamma_{\text{in}}. \tag{S18}$$

At the interface Γ_{int} we use a no-slip condition for the velocity and transmission conditions for the temperature

$$u = 0, \quad T_{\text{gas}} = T_{\text{steel}}, \quad \kappa_{\text{gas}}\, \partial_n T_{\text{gas}} = \kappa_{\text{steel}}\, \partial_n T_{\text{steel}}, \quad \rho\left(V^c Y_k - D_{k,\text{mix}} \nabla Y_k\right) \cdot n = 0 \quad \text{on } \Gamma_{\text{int}}. \tag{S19}$$

Here, n denotes the outer unit normal vector at the boundary and $\partial_n f = \nabla f \cdot n$ is the normal derivative of some scalar function f. Additionally, for a vector valued function v, we denote by $\partial_n v = Dv\, n$ the application of the Jacobian Dv to the normal vector n. At the outer wall of the reactor, we use homogeneous Neumann conditions

$$\rho\left(V^c Y_k - D_{k,\text{mix}} \nabla Y_k\right) \cdot n = 0, \qquad \partial_n T = 0 \qquad \text{on } \Gamma_{\text{wall}}. \tag{S20}$$

We have the following symmetry conditions on Γ_{sym}

$$u \cdot n = 0 \quad \mu\, \partial_n u \times n = 0, \qquad \rho\left(V^c Y_k - D_{k,\text{mix}} \nabla Y_k\right) \cdot n = 0, \qquad \partial_n T = 0 \qquad \text{on } \Gamma_{\text{sym}}. \tag{S21}$$

Finally, for the outlets we use the conditions

$$\mu\, \partial_n u - pn = 0, \qquad \rho\left(V^c Y_k - D_{k,\text{mix}} \nabla Y_k\right) \cdot n = 0, \qquad \partial_n T = 0 \qquad \text{on } \Gamma_{\text{out}}. \tag{S22}$$

As initial conditions at $t = 0$, we specify the initial gas composition and temperature (denoted by the superscript "0"):

$$Y_k(0,\cdot) = Y_k^0, \qquad T(0,\cdot) = T^0 \qquad \text{in } \Omega. \tag{S23}$$

1.2 Identification of Reaction Kinetics

The ammonia decomposition reaction measurements used for kinetic modeling are carried out in an electrically heated screening reactor with 14 parallel microchannels with a circular cross section with a radius of 250 μm and a length of 25 mm containing 20 mg of homemade Ni-based catalyst layers under 5 bar pressure from 500°C to 700°C, which was controlled by a thermocouple placed in the center of the reactor. The feed consists of 90 mol-% pure anhydrous ammonia sourced from Linde Gas AG at a purity class of 3.8 and 10 mol-% argon as internal standard. Kinetic measurements were performed with a gas

hourly space velocity (GHSV) between 1,132,000 1/h and 3,395,000 1/h. The product effluents from the reactor were analyzed quantitatively by on-line Fourier-transformation infrared spectroscopy (FTIR) and gas chromatography. Unconverted ammonia in the gas stream leaving the test rig was removed by an adsorber bed filled with the molecular sieve 13X from GIEBEL FilTec, Bretzfeld-Schwabbach (Germany) to ensure an environmentally safe operation.

To model the ammonia decomposition reaction, we use the results of the experiments described above to numerically identify a set of parameters for the reaction kinetics. Our model is based on the one presented in Section 2.2 of the main article with only minor modifications. Because the experiments are carried out isothermally, we use an isothermal model for the reactor, i.e., we drop the temperature equation (13) and assume that the reactor is at a defined constant temperature. Additionally, we use a one-dimensional model for the reactor, which is very similar to the one discussed in the previous work [1] and we refer to this publication for more details.

To obtain a suitable fit for the model, we solve the following parameter identification problem

$$\min_{y,u_c} J\,(y,u_c) = \sum_i \int_{\Gamma_{\text{out}}} \left(\chi_{\text{sim},i}^{\text{NH}_3} - \chi_{\text{exp},i}^{\text{NH}_3}\right)^2 \,\mathrm{d}s \tag{S24}$$

subject to (7) and (8).

Here, the vector $u_c = \left[\log(A)\,, E_a, m_{\text{emp}}\right]^T$ denotes the optimization variables, which are the parameters describing the reaction kinetics. The state variables are given by $y = [p, u, Y]^T$, where Y is a vector containing Y_k in component k. Finally, the simulated and measured ammonia conversion are denoted by $\chi_{\text{sim},i}^{\text{NH}_3}$ and $\chi_{\text{exp},i}^{\text{NH}_3}$, respectively, for experiment i. Ammonia conversion is defined as

$$\chi^{\text{NH}_3} = 1 - \frac{Y_{\text{NH}_3}}{Y_{\text{NH}_3}^{\text{in}}}, \tag{S25}$$

where $Y_{\text{NH}_3}^{\text{in}}$ denotes the inlet mass fraction of NH_3. The aim of Eq. (S24) is to identify parameters for the reaction kinetics so that the difference between the simulated and measured ammonia conversion is minimized in a least-squares sense.

To solve this problem numerically, we use our optimization software cashocs [2], which is based on the finite element software FEniCS [3]. It solves such parameter identification problems by applying a variational adjoint approach. For more details, we refer to [2], where the software is presented, and [1], where it is used to solve a similar parameter identification problem. For the numerical parameter identification, we apply a limited memory BFGS method implemented in cashocs. The obtained results are discussed in the following section.

2 Additional Results and Discussion

2.1 Calibrating Simulation and Experiment

The parameters obtained by the identification process explained in Section 1.2 are shown in Table 1. In Figure 8 the simulated and measured conversion rates are shown over the temperature for various values of the weighted hourly space velocity (WHSV), i.e., for various flow rates. We observe that there is a good agreement between measurements and our simulation, with only some minor discrepancies. This is reinforced by the results shown in Figure 9, where the simulated and measured NH_3 conversion rates are compared in a parity plot. Additionally, the coefficient of determination between simulation and experiment is $R^2 = 0.986$, which indicates that we have obtained a very good fit, closely fitting our simulation to the experimentally obtained results. Hence, we use the identified parameters for simulating our surrogate model (cf. Section 2.5 in the manuscript).

Table 1. Identified reaction kinetics parameters.

Parameter	Name	Value	Unit
E_a	Activation Energy	163766.5	$\frac{\mathrm{J}}{\mathrm{mol}}$
$\log(A)$	Logarithm of pre-exponential factor	25.9	dimensionless
m_{emp}	Empirical Exponent	0.4075	dimensionless

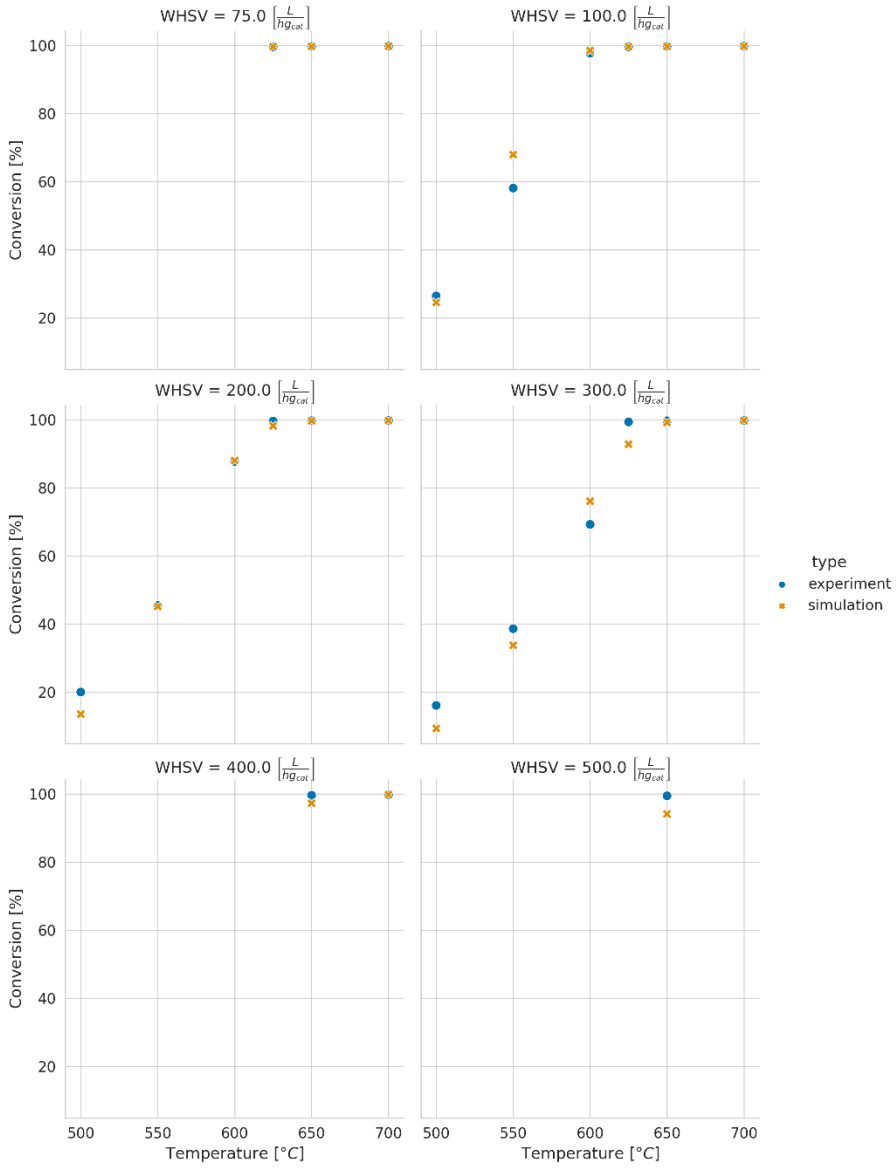

Figure 8. Comparison of simulated and measured conversion rates for various values of the WHSV.

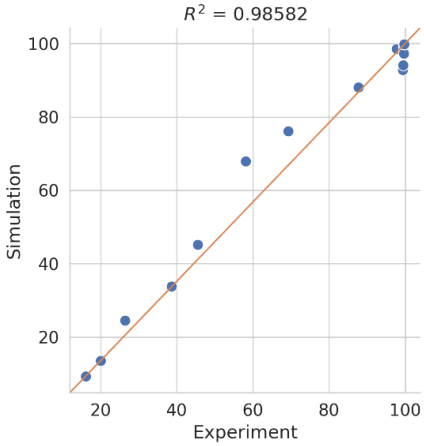

Figure 9. Parity plot of simulated and measured ammonia conversion rates for all experiments.

2.2 Flow Characteristics of the Reactor

In Figure 10, we plot the gas velocity for each of the DEC and AFB channels in one layer of the reactor. Note that the plots only show the maximum velocity for each channel, which is proportional to the flow rate as all channels have the same dimensions. Particularly for the DEC channels, we observe that the flow rate distribution is much more uniform in the DEC part compared to the AFB part. In the latter part, the flow distribution is shown to be divided into six major flow regions, which is due to the structure of the in- and outlets of the AFB channels (cf. Figure 11). These results justify our assumption in Section 2 of the main document, where we assume to have a uniform flow distribution among the reactors channels. Additionally, we show the pressure distributions for the DEC and AFB parts in Figure 11.

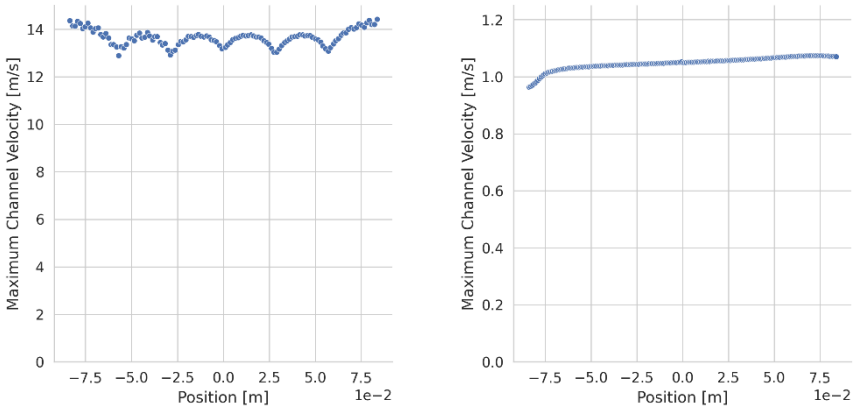

Figure 10. Gas velocity over the channels for the AFB part (left) and DEC part (right).

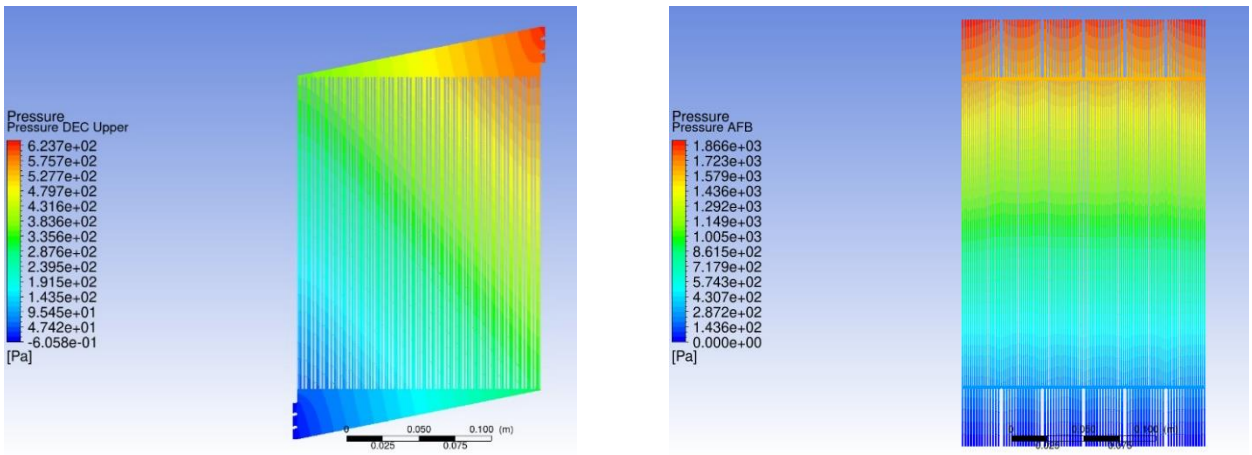

Figure 11. Pressure distribution in the DEC part (left, flow from top right to lower left) and AFB part (right, flow from top to bottom).

2.3 Detailed Efficiencies for Alternative Ammonia Cracking Systems

The laboratory scale e-cracker by Hogg NH3 Systems [4] has specific power demands of 14 MW/t_{H2} and an output level of up to 8.5 Nm³/h cracked gas consisting of 74.96 mol-% hydrogen, 24.99 mol-% nitrogen and 500 ppm (molar) ammonia, equivalent to an efficiency of 77.4%.

The cracking system by the Danish company Topsoe has an output level of > 5 MTPD (metric tons per day) hydrogen at a specific power demand of 6-8 MW/t_{H2}, resulting in an efficiency of up to 94.4% [5]. If the hydrogen is purified by PSA, the efficiency decreases to 73.6%, assuming a hydrogen recovery of 78% in the PSA unit. If the hydrogen is converted to electricity in a low-temperature PEM fuel cell, the complete process chain from ammonia to electric power, reaches an efficiency of 40.5%.

Perna et al. [6] can produce 8.33 kg/h of pure hydrogen from 77.25 kg/h of ammonia, resulting in an efficiency of 68.8%. The complete process chain from ammonia to electricity has an efficiency of 35.8%, assuming a fuel excess ratio at the anode λ_A of 1.01 and an electric efficiency of the fuel cell of 52%.

The cracker developed by the University of Duisburg-Essen together with the hydrogen and fuel cell center ZBT GmbH has an efficiency of up to 114.5% and the complete process chain reaches an efficiency of up to 57.0% [7]. The efficiency of the fuel processor with a value greater than 100% results from the definition of the efficiency itself, cf. Eq. 16 in the manuscript. If the heat required for the decomposition reaction can be fully supplied by the anode off-gas of the fuel cell, the efficiency is only determined by the change in the amount of substance in the decomposition reaction. According to reaction equation (1) in the manuscript, 2 moles of ammonia in the feed will yield 3 moles of hydrogen. Multiplying these values by their respective lower heating value results in the mentioned efficiency of 114.5%. It should be noted that this efficiency can only be achieved for certain fuel utilization ratios of the fuel cell, the presence of which is also mandatory.

The Israeli company GenCell Ltd. sells a 4 kWe containerized off-grid power generator based on ammonia cracking and alkaline fuel cell technology for telecom applications [8]. The fuel consumption is indicated as up to 2.5 kg of ammonia per hour, resulting in a system efficiency of 31.0%.

References

[1] S. Blauth, C. Leithäuser, R. Pinnau, *J. Eng. Math.* **2021**, *128 (1)*. DOI: https://doi.org/10.1007/s10665-021-10134-2

[2] S. Blauth, *SoftwareX* **2021**, *13*, 100646. DOI: https://doi.org/10.1016/j.softx.2020.100646

[3] M. Alnaes, J. Blechta, J. Hake, A. Johansson, B. Kehlet, A. Logg, C. Richardson, J. Ring, M. E. Rognes, G. N. Wells, *Archive of numerical software* **2015**, *3 (100)*, 9 – 23.

[4] http://www.james-hogg.com/ht1_cracker_datasheet.pdf (Accessed on September 05, 2023).

[5] R. Nielsen, *Topsoes Ammonia cracking technology – Delivering green Hydrogen* **2021**.

[6] A. Perna, M. Minutillo, S. Di Micco, V. Cigolotti, A. Pianese, *E3S Web Conf.* **2020**, *197*, 5001. DOI: https://doi.org/10.1051/e3sconf/202019705001

[7] F. E. Nigbur, *Ammoniak-Cracker zur Brenngasversorgung von Brennstoffzellen*, Dissertation, Universität Duisburg-Essen.

[8] https://www.gencellenergy.com/our-products/gencell-a5/ (Accessed on September 05, 2023).